

Suppression of radiation loss in high kinetic inductance superconducting co-planar waveguides

S. Hähnle,^{1,2,a)} N. v. Marrewijk,² A. Endo,^{2,3} K. Karatsu,^{1,2} D. J. Thoen,² V. Murugesan,¹ and J. J. A. Baselmans^{1,2}

¹⁾*SRON - Netherlands Institute for Space Research, Sorbonnelaan 2, 3584 CA Utrecht, The Netherlands*

²⁾*Department of Microelectronics, Faculty of Electrical Engineering, Mathematics and Computer Science (EEMCS), Delft University of Technology, Mekelweg 4, 2628 CD Delft, The Netherlands*

³⁾*Kavli Institute of NanoScience, Faculty of Applied Sciences, Delft University of Technology, Delft, The Netherlands.*

We present a lab-on-chip technique to measure the very low losses in superconducting transmission lines at (sub-) mm wavelengths. The chips consist of a 100 nm thick NbTiN Coplanar Waveguide (CPW) Fabry-Pérot (FP) resonator, coupled on one side to an antenna and on the other side to a Microwave Kinetic Inductance detector. Using a single frequency radiation source allows us to measure the frequency response of the FP around 350 GHz and deduce its losses. We show that the loss is dominated by radiation loss inside the CPW line that forms the FP and that it decreases with decreasing line width and increasing kinetic inductance as expected. The results can be quantitatively understood using SONNET simulations. The lowest loss is observed for a CPW with a total width of 6 μm and corresponds to a Q-factor of $\approx 15,000$.

Superconducting transmission lines, such as co-planar waveguides (CPWs) or microstrips, are increasingly prevalent for cryogenic high-frequency applications upwards of 100 GHz, such as on-chip spectrometers¹⁻³, phased array antennas⁴ and kinetic inductance parametric amplifiers⁵. These applications require ultra low-loss transmission lines with a loss tangent of $\tan \delta \lesssim 10^{-3}$ and lengths upwards of 100λ , either as an integral part of the circuit in kinetic inductance parametric amplifiers or phased array antennas, or as a connecting element in on-chip spectrometers. Microstrip losses in this frequency range down to $\tan \delta = 2 \times 10^3$ have been measured previously⁶. Here, we focus on losses in CPW. CPW lines have an advantage over microstrip lines in that they do not require a deposited dielectric, which is a source of loss, decoherence and noise. However, CPWs are open structures and can radiate power, which is a source of loss and increases cross coupling to neighboring lines. The dominant radiation loss mechanism is the so-called leaky mode, which is present if the phase velocity in the line exceeds the phase velocity in the substrate. For microwave applications, this can be controlled by reducing the line width, but this becomes increasingly impractical at mm- and sub-mm wavelengths. In superconducting lines, the phase velocity is reduced due to kinetic inductance, which in principle allows to create a line with a phase velocity below the substrate phase velocity, thereby eliminating the leaky mode radiation and creating ultra low-loss transmission lines at frequencies exceeding hundreds of GHz. Dielectric losses in microstrips at frequencies up to 100 GHz have been measured previously⁶. In this paper, we demonstrate lab-on-chip loss measurements of superconducting NbTiN CPW Fabry-Pérot resonators around 350 GHz. We show that the radiation loss can be reduced and even virtually eliminated by reducing the phase velocity, which is accomplished by narrowing the CPW

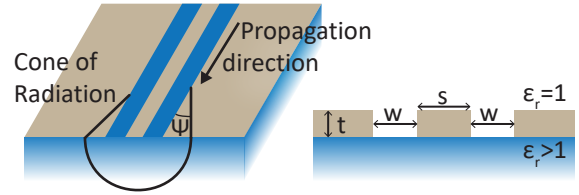


FIG. 1. a) CPW geometry. b) Cone of radiation emitted along the propagation direction of the CPW mode, with radiation angle Ψ .

line to a total width of $\lesssim 6 \mu\text{m}$.

The effective dielectric constant of a transmission line using a perfect electric conductor (PEC) is given by

$$\epsilon_{eff} = c^2 LC \quad (1)$$

where c is the speed of light and L and C are the transmission line inductance and capacitance per unit length respectively. In a CPW as shown in Fig. 1, this can be approximated by

$$\epsilon_{eff} \approx \frac{\epsilon_r + 1}{2} \quad (2)$$

with the dielectric constant of the substrate ϵ_r . The phase velocity $v_{ph} = \frac{c}{\sqrt{\epsilon_{eff}}}$ in the guided CPW mode is therefore faster than in the substrate. This creates a shockwave in the substrate, leading to a radiation cone characterized by the radiation angle Ψ (see Fig. 1). The frequency dependent loss factor α at high frequencies due to this shockwave has been derived by Frankel et al.⁷ from the electric and magnetic field distributions in the dielectric materials due to the current distribution in a PEC as

$$\alpha_{rad} = \left(\frac{\pi}{2}\right)^5 2 \left(\frac{(1 - \cos^2(\Psi))^2}{\cos(\Psi)} \right) \frac{(s + 2w)^2 \epsilon_r^{3/2}}{c^3 K(\sqrt{1 - k^2}) K(k)} f^3 \quad (3)$$

where s and w are the CPW line and slot width, $k = s/(s + 2w)$ and $K(k)$ is the complete elliptical integral of the first kind. It

^{a)}s.haehnle@sron.nl

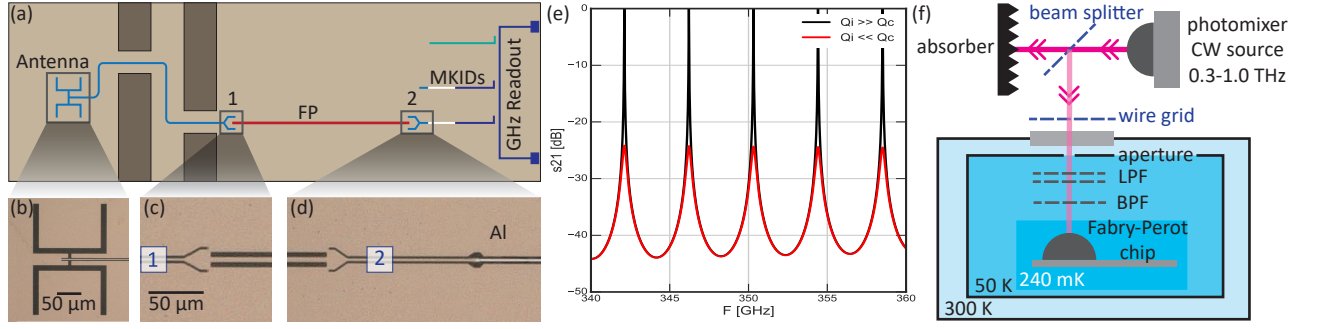


FIG. 2. a) Chip schematic. b) Picture of antenna. c) Picture of first coupler. d) Picture of second coupler, including the transition to the Aluminum section of the MKID. e) Simulated Fabry-Pérot transmission. f) Experimental setup schematic. The filterstack consists of Low-pass filters (LPF) and a bandpass filter (BPF). The aperture plane is at the 50K window and a polarizing wire grid is located outside the cryostat.

can be seen in Eqn.3, that the magnitude of radiation loss is strongly dependent on Ψ which is given by the discrepancy of the dielectric constants

$$\cos(\Psi) = \frac{\sqrt{\epsilon_{eff}(f)}}{\sqrt{\epsilon_r}}. \quad (4)$$

For a PEC CPW, this ratio is only dependent on the substrate and independent of the conductor properties. However, in a superconducting CPW, the kinetic inductance per unit length L_k due to the inertia of Cooper pairs needs to be taken into account, changing Eqn. 1 to

$$\epsilon_{eff} = c^2(L_g + L_k)C \quad (5)$$

where the transmission line inductance is the sum of its kinetic inductance and geometric inductance L_g .

Conceptually, using a CPW with high L_k leads to a suppression of the radiation loss, as the radiative angle Ψ is reduced. If L_k is sufficiently large to obtain $\epsilon_{eff} \geq \epsilon_r$, the radiative shockwave does not form as the phase velocity of the CPW line is slower than in the substrate, resulting in theoretically zero radiation loss. The kinetic inductance L_k increases with the film normal state sheet resistance, a reduced film thickness (in the regime of thin films compared to the penetration depth) and with reducing linewidth. A CPW of a 100 nm NbTiN film of in total 6 μm wide will fulfill the condition that $\epsilon_{eff} > \epsilon_r$ (see supplementary material). Another method is to use a CPW fabricated on a vanishingly thin dielectric membrane, which can be approximated as a free standing CPW and therefore does not radiate.

Measuring the radiation loss of a superconducting CPW at sub-mm wavelengths requires a highly sensitive device, capable of measuring a loss tangent $\tan \delta < 10^{-3}$. For this purpose we design a chip with a Fabry-Pérot resonator at its core, as shown in the schematic of 2a). A similar device has been used by Göppl et al.⁸ at microwave frequencies.

The Fabry-Pérot (FP) resonator is a single CPW line terminated by two identical couplers on either end, with the resonance condition

$$F_n = n \frac{c}{2L_{FP}\sqrt{\epsilon_{eff}}} \quad (6)$$

where ϵ_{eff} is the effective dielectric constant of the CPW, L_{FP} is the resonator length and n is the mode number. Transmission through the resonator can be described as a series of Lorentzian peaks, where each peak has a loaded Quality factor Q_L given by the resonance frequency and FWHM (full width at half maximum)

$$Q_L = \frac{F_n}{\text{FWHM}_n}. \quad (7)$$

The loaded Q-factor is a measure of the power loss per cycle which can be separated in its two primary components:

$$\frac{1}{Q_L} = \frac{1}{Q_c} + \frac{1}{Q_i} \quad (8)$$

First, Q_c is the power leakage through the two couplers

$$Q_c(n) = \frac{n\pi}{|S_{2'1'}|^2} \quad (9)$$

where $|S_{2'1'}|^2$ is the transmission through a single coupler with ports 1' and 2' (see the supplementary material). Second, the internal losses described by Q_i which is defined as

$$Q_i = \frac{\beta}{2\alpha} \quad (10)$$

with the propagation constant $\beta = 2\pi/\lambda$ and the loss factor α , where $[\alpha] = \text{Np/m}$. The loss inside the resonator is given by the combination of ohmic loss ($Q_{i,ohm}$), dielectric loss ($Q_{i,die}$) and radiation loss of the CPW ($Q_{i,rad}$), as well as radiation loss at the coupler ($Q_{i,coup}$):

$$\frac{1}{Q_i} = \frac{1}{Q_{i,ohm}} + \frac{1}{Q_{i,die}} + \frac{1}{Q_{i,rad}} + \frac{1}{Q_{i,coup}} \quad (11)$$

Since Q_L is the measured variable, a precise measurement of Q_i requires exact knowledge of Q_c , which is experimentally difficult due to fabrication constraints. Therefore, measurements in the internal loss dominated regime of $Q_c > Q_i$ are preferred, since then $Q_L \approx Q_i$ (see Eqn.8). However Q_c cannot be increased arbitrarily, as this will reduce the Lorentzian peak height according to

$$|S_{21}|_{\max} = \frac{Q_L}{Q_c}, \quad (12)$$

as shown in Fig 2e). Additionally, we use in the experiments a source with limited frequency resolution, limiting the design range of Q_c as well. Taking these considerations into account, all chips discussed in this paper are designed in Sonnet⁹ to have $Q_c^{design} = 2.7 \times 10^4$ at 350 GHz (see the supplementary material). The center frequency of 350 GHz is chosen based on the available experimental setup.

In order to measure the CPW radiation loss dependency on ϵ_{eff} in eqs.(3) and (4), four chips are designed with varying linewidths w and slotwidths s of the Fabry-Pérot lines as given in Table I. All chips are fabricated on a single 350 μm thick Sapphire wafer, ensuring common film properties across the chips. The 100 nm NbTiN film is deposited directly on the Sapphire using reactive sputtering of a NbTi target in a Nitrogen-Argon atmosphere¹⁰. Details on the fabrication can be found in Endo et al.¹¹, which follows the same route as this paper.

The measured line geometry is determined via SEM (Scanning Electron Microscope) inspection and deviates slightly due to overetch in the fabrication process. Using the surface inductance of $L_s = 1.03$ pH at 350 GHz calculated from the measured film parameters ($T_c = 14.7$ K, $\rho_N = 102$ $\mu\Omega\text{cm}$), and the known parameters of the C-plane Sapphire substrate ($\epsilon_r^C = 11.5$; $\epsilon_r^{AB} = 9.3$), we obtain the measured values of ϵ_{eff} at 350 GHz given in Table I. NbTiN parameters are measured on a test sample close to the FP resonators to eliminate effects of spatial variations in the NbTiN properties¹⁰. The resonator length is $L_{FP} = 10$ mm, corresponding to mode numbers in the range of 60-90 for the four chips.

A first estimate of the radiation loss, naively using Eqn.5 in Eqn.3 to account for the kinetic inductance, ranges from $Q_i = 5.6 \times 10^3$ for the 5 μm line to $Q_i = 5.4 \times 10^6$ for the 3 μm line; for the 2 μm line, the equation diverges.

Using Mattis-Bardeen theory¹², we can estimate the ohmic losses to be multiple orders of magnitude higher than the stated loss, which means that radiation loss dominates for $w = s > 2\mu\text{m}$. It has been shown previously, that highly disordered superconductors start to deviate from Mattis-Bardeen theory¹³ for high frequencies ($f > 0.3\Delta$) and high normal-state resistivity ($\rho_N > 100\mu\Omega\text{cm}$). However, both the frequency range of this experiment and the NbTiN film resistivity are at the lower limit and only a minimal deviation is expected.

In order to drive the FP resonator, one coupler (port 1) is connected via a CPW with $w = 2$ μm and $s = 2$ μm to a double-slot antenna, centered at 350 GHz. The other coupler (port 2) is directly attached to the shorted end of a Microwave Kinetic Inductance Detector (MKID), which is a $\lambda/4$ res-

onator with $F_{res} \approx 6.5$ GHz based on the hybrid CPW design introduced by Janssen et al.¹⁴. In the MKID, a 1.5 mm long, narrow hybrid CPW with a NbTiN ground plane and an Al ($\Delta_{Al} \approx 90\text{GHz}$ $T_c = 1.28$ K) center line follows directly after a NbTiN coupler section as shown in Fig. 2d). Incoming THz radiation is absorbed in the low bandgap Al line, thereby creating quasiparticles which changes the kinetic inductance of the film. This causes a frequency shift of the MKID resonator which is read out with the SPACEKIDS microwave readout¹⁵.

Additional MKIDs, which are not coupled to the Fabry-Pérot and hereafter referred to as blind MKIDs, are placed on the chip as reference detectors. A microwave resonator with the same CPW geometry as the FP resonator is also added (green line in Fig. 2a)). Sampling the full FP transmission requires a measurement with a dynamic range of ≈ 50 dB (see Fig. 2e)). In order to reduce stray light reaching the MKIDs, the copper holder in which the chip is placed contains a labyrinth structure as indicated in Fig. 2a), separating the chips exposed antenna section from the dark Fabry-Pérot section. Additionally, a low- T_c backside layer of beta-Ta is deposited on the chip backside and acts as a stray light absorber¹⁶.

In the experiment we mount an 8 mm Si lens on the chip backside, centered on the antenna, and place both in the Cu sample holder. This is placed on the cold stage of a He-3/He-4 sorption cooler¹⁷, as shown in Fig. 2f), operating at $T \approx 250$ mK. A commercial photomixer continuous wave (CW) source¹⁸ is positioned at room temperature and coupled into the cryostat via a beamsplitter to reduce the incoming power and avoid saturation of the MKIDs. The source emits a linear polarized, single frequency signal which is tunable in the range of 0.1...1.2 THz with a minimum step size of ~ 10 MHz and an absolute frequency accuracy of < 2 GHz. A band pass filter stack centered at $F_c = 346$ GHz and > 20 dB out of band suppression is located in the cryostat with a polarizing wire grid mounted on the vacuum window.

The FP transmission of the four chips is measured by sweeping the CW source from 310 GHz to 380 GHz in 10 MHz steps with an integration time of 1 s and detecting the resulting MKID response. An electrical on/off modulation of the CW source at $f_{mod} = 11.97$ Hz is employed to avoid $1/f$ noise. As the CW output power and beam shape are not well known, the absolute coupling strength to the MKID is not measured and the given responses are relative to the noise floor. However, the detector linearity in the measurement range was confirmed by measuring at various CW powers and retrieving identical results for the FP peak shapes.

The resulting response S_D of the FP-coupled MKID, shown in Fig. 3a) exemplary for chip I, clearly shows the expected regular spaced peaks of the FP resonator combined with a strongly frequency dependent baseline. The blind MKIDs spectrum S_B shows the same baseline but with a frequency independent offset O compared to S_D . As the same baseline is present in both detectors, we attribute it to CW power directly coupling to the MKIDs. Its frequency dependence is given by inherent fluctuations of the CW source combined with the bandpass filter transmission, both of which are also present in the Fabry-Pérot transmission, while the constant offset is

	$w_d = s_d$ [μm]	s_{meas} [μm]	w_{meas} [μm]	ϵ_{eff}
Chip I	2	1.95	2.15	13.1
Chip II	3	2.95	3.15	10.9
Chip III	4	3.95	4.15	9.5
Chip IV	5	4.95	5.15	9.0

TABLE I. Designed and measured slot width w and line width s and resulting ϵ_{eff} for each chips Fabry-Pérot resonator.

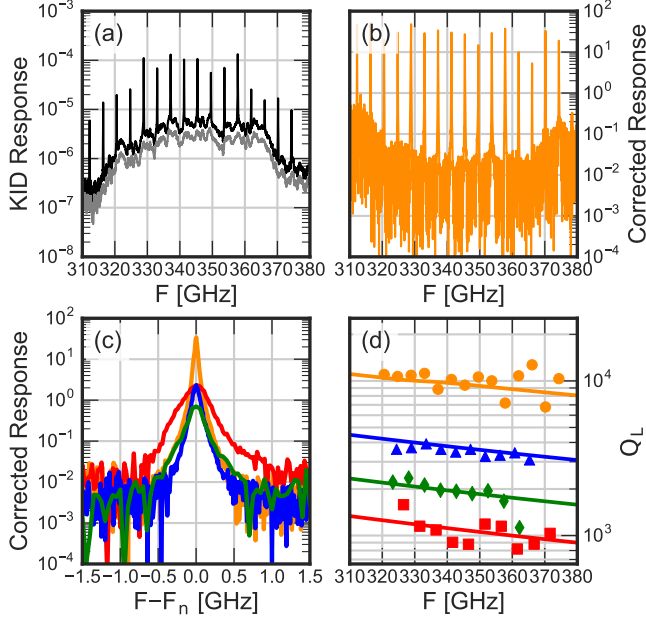


FIG. 3. (a) Measured spectrum for chip I of the Fabry-Pérot coupled MKID (black) and the blind MKID (grey). (b) Corrected spectrum of the FP coupled MKID of chip I. (c) Example peaks of the corrected spectra of each chip (I: orange; II: blue; III: green; IV: red) (d) Measured Q_L for all chips and as symbols and simulated $Q_{L,sim}$ as lines, using the previous defined color scheme.

due to the difference in MKID responsivity. We retrieve the corrected FP transmission S_{FP} shown in Fig. 3b) using

$$S_{FP} = S_D / S_B - O \quad (13)$$

where O is determined in the regions between FP peaks where S_D is dominated by the direct coupling.

A comparison between the FP peaks of the 4 chips (see Fig. 3c) shows sharper and higher peaks for narrower CPWs. This already indicates lower losses for the narrow CPWs, as the experiments were designed for the Q_i -limited regime ($Q_L \approx Q_i$). The peak height difference for chip IV is due to the use of a different aperture, which only affects the direct CW coupling and not the resonance Q factor.

In order to obtain Q_L the individual peaks are fitted with a Lorentzian function

$$L_n(F) = I \frac{Q_{L,n}^2}{Q_{L,n}^2 + 4 \left(\frac{F - F_n}{F_n} \right)^2} + O_L \quad (14)$$

with peak height I and offset O_L , and the fit results plugged into Eqn.7. The fitted Q_L is shown in Fig. 3d) as dots and compared to simulations shown by lines.

The simulations are carried out in Sonnet (see the supplementary material) and are based on the measured CPW geometry and NbTiN properties as discussed previously. An excellent agreement with the measured data is found by including the coupling strength S_{21} and radiation loss of the CPW in these simulations. The observed frequency dependence of Q_L is due to both the changing coupling strength and

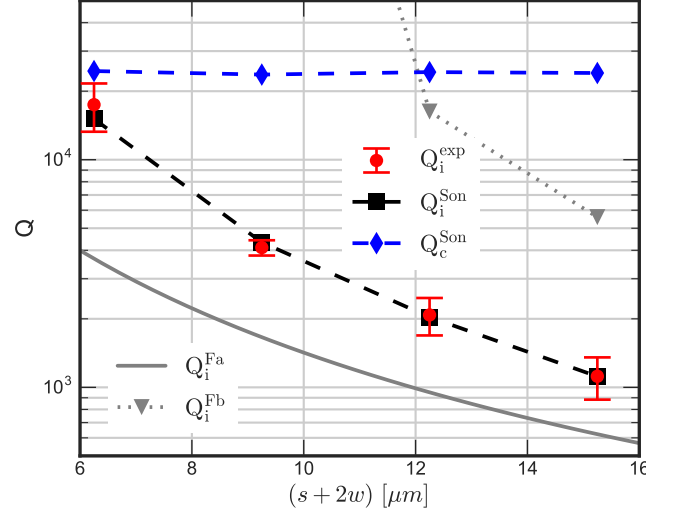


FIG. 4. Measured Q_i^{exp} compared with sonnet simulations for internal loss Q_i^{son} and coupling strength Q_c^{chip} , as well as analytical solutions for a PEC CPW Q_i^{Fa} and superconducting CPW Q_i^{Fb} .

line loss $\alpha \propto f^3$, while the oscillation in measured Q_L can be explained qualitatively by a standing wave before the first FP coupler with a resonance length $L_{sw} > L_{FP}$.

In order to extract the internal loss from the measured Q_L , the Q_c must be known. While it is in principle possible to measure Q_c directly using the analysis in Fig. 2e), this requires a dynamic range > 50 dB or an absolute calibration of the S_{21} at the resonance peaks, both of which are not possible in our experimental system. Therefore, we use the Sonnet simulations of the coupler to obtain Q_c .

We then average over all peaks in the frequency range to retrieve Q_i^{exp} at 350 GHz, shown in Fig. 4, which is in excellent agreement with the Sonnet simulations of the CPW radiation loss. It is significantly higher than the analytical solution Q_i^{Fa} for the case of a PEC using Eqn.3, with the difference increasing for narrower lines up to a factor of 4. However, it is also significantly lower than the naive approach of substituting the superconducting ϵ_{eff} of Eqn. 5 into Eqn.3 resulting in Q_i^{Fb} . All four CPW geometries are within the validity range for Eqn.3, but as the derivation of Eqn.3 is based on a planar PEC geometry, and does not take a superconductor into account, it is not surprising that both of these approaches fail. For Q_i^{Fa} the phase velocity change due to the kinetic inductance is completely neglected, while the naive inclusion of L_k in ϵ_{eff} for Q_i^{Fb} , while correct for phase velocity considerations, does not take into account the actual field distribution in the dielectric. The Q_i of the NbTiN microwave resonator located on each of the chips is measured to be $\approx 2 \times 10^6$, which is consistent with previous experiments¹⁹ and indicates no issues with film quality.

In addition to the quantitative disagreement between the experiment and the analytic solution, we find a non-zero loss for chip I where we expect no radiation loss according to the shockwave model. As $\epsilon_{eff} > \epsilon_r$ is a fundamental argument

against radiation loss due to a shockwave, a different mechanism must be considered. Radiation loss due to the strong fields at the open ended couplers were found to have a negligible contribution in sonnet simulations with $Q \approx 10^5$ (see supplementary material). Dielectric losses due to the crystalline sapphire substrate are expected to be negligible and can be excluded due to the high Q_i of the microwave resonator. Ohmic losses due to disorder effects in the NbTiN film are expected to be much smaller than observed and are not compatible with the measured width dependence. Additionally, none of these losses are included in the simulation for Q_i^{son} , where we find a quantitative agreement with the measurements. Due to this excellent agreement, we speculate that we are limited by a different loss mechanism, most likely due to the fundamentally unconfined nature of the CPW mode.

In conclusion, we have designed, fabricated and measured superconducting on-chip CPW Fabry-Pérot resonators with high kinetic inductance NbTiN ($L_s = 1.03/\text{pH}$) and multiple line dimensions at frequencies from 320 to 380 GHz. We find a line width dependence for the internal loss Q_i , with values of $(1.1 \pm 0.2) \times 10^3$ for a total line width of $15.25 \mu\text{m}$ to $(1.7 \pm 0.4) \times 10^4$ for $6.25 \mu\text{m}$, corresponding to $\alpha = 0.007 \text{ dB/mm}$ and $\alpha = 0.09 \text{ dB/mm}$ respectively. The measured loss is in quantitative agreement with simulations of the radiation loss using Sonnet. However, the analytical solution by Frankel et al.⁷ is not valid in the regime of high-kinetic inductance superconductors, underestimating the CPW loss when $\epsilon_{eff} \approx \epsilon_r$.

Furthermore, we show that the on-chip Fabry-Pérot resonator provides a sensitive and highly flexible method for high- Q_i transmission line loss measurements at sub-mm wavelengths. Extensions to other transmission line types, such as microstrips, can be easily achieved by modifying the resonator line and couplers, while the antenna can be exchanged to fit the required frequency range. Further optimization in the quasi-optical path and chip design are viable paths to improve the dynamic range and reduce effects from standing waves. For measurements of narrower lines where even lower losses are expected, a THz source with higher frequency resolution, such as multipliers, is required.

See supplementary material for the analytic characterization of a superconducting CPW and a comprehensive discussion of the Sonnet simulations for the Fabry-Pérot resonators.

The authors thank A. Neto for the helpful discussions. This work is supported by the ERC COG 648135 MOSAIC. A. Endo, N.v. Marrewijk, and K. Karatsu were supported by the Netherlands Organization for Scientific Research NWO (Vidi grant No. 639.042.423)

The data that support the findings of this study are available from the corresponding author upon reasonable request.

¹A. Endo, K. Karatsu, Y. Tamura, T. Oshima, A. Taniguchi, T. Takekoshi, S. Asayama, T. J. L. C. Bakx, S. Bosma, J. Bueno, K. W. Chin, Y. Fujii, K. Fujita, R. Huiting, S. Ikarashi, T. Ishida, S. Ishii, R. Kawabe, T. M. Klapwijk, K. Kohno, A. Kouchi, N. Llombart, J. Maekawa, V. Murugesan, S. Nakatsubo, M. Naruse, K. Ohtawara, A. Pascual Laguna, J. Suzuki,

K. Suzuki, D. J. Thoen, T. Tsukagoshi, T. Ueda, P. J. de Visser, P. P. van der Werf, S. J. C. Yates, Y. Yoshimura, O. Yurduseven, and J. J. A. Baselmans, *Nature Astronomy* **3**, 989 (2019), arXiv:1906.10216 [astro-ph.IM].

²G. Cataldo, E. M. Barrentine, B. T. Bulcha, N. Ehsan, L. A. Hess, O. Noroozian, T. R. Stevenson, K. U-Yen, E. J. Wollack, and S. H. Moseley, *Journal of Low Temperature Physics* **193**, 923 (2018).

³E. Shirokoff, P. S. Barry, C. M. Bradford, G. Chattopadhyay, P. Day, S. Doyle, S. Hailey-Dunsheath, M. I. Hollister, A. Kovcs, C. McKenney, H. G. Leduc, N. Llombart, D. P. Marrone, P. Mauskopf, R. O'Brien, S. Padin, T. Reck, L. J. Swenson, and J. Zmuidzinas, in *Millimeter, Submillimeter, and Far-Infrared Detectors and Instrumentation for Astronomy VI*, Vol. 8452, edited by W. S. Holland, International Society for Optics and Photonics (SPIE, 2012) pp. 209 – 219.

⁴P. A. R. Ade, R. W. Aikin, M. Amiri, D. Barkats, S. J. Benton, C. A. Bischoff, J. J. Bock, J. A. Bonetti, J. A. Brevik, I. Buder, E. Bullock, G. Chattopadhyay, G. Davis, P. K. Day, C. D. Dowell, L. Duband, J. P. Filippini, S. Fliescher, S. R. Golwala, M. Halpern, M. Hasselfield, S. R. Hildebrandt, G. C. Hilton, V. Hristov, H. Hui, K. D. Irwin, W. C. Jones, K. S. Karkare, J. P. Kaufman, B. G. Keating, S. Kefeli, S. A. Kernasovskiy, J. M. Kovac, C. L. Kuo, H. G. LeDuc, E. M. Leitch, N. Llombart, M. Lueker, P. Mason, K. Megerian, L. Moncelsi, C. B. Netterfield, H. T. Nguyen, R. O'Brien, R. W. O. IV, A. Orlando, C. Pryke, A. S. Rahlén, C. D. Reintsema, S. Richter, M. C. Runyan, R. Schwarz, C. D. Sheehy, Z. K. Staniszewski, R. V. Sudiwala, G. P. Teply, J. E. Tolan, A. Trangsud, R. S. Tucker, A. D. Turner, A. G. Vieregge, A. Weber, D. V. Wiebe, P. Wilson, C. L. Wong, K. W. Yoon, and J. Z. and, *The Astrophysical Journal* **812**, 176 (2015).

⁵B. Ho Eom, P. K. Day, H. G. LeDuc, and J. Zmuidzinas, *Nature Physics* **8**, 623 (2012).

⁶J. Gao, A. Vayonakis, O. Noroozian, J. Zmuidzinas, P. Day, and H. Leduc, **1185** (2009), 10.1063/1.3292306.

⁷M. Y. Frankel, S. Gupta, J. A. Valdmanis, and G. A. Mourou, *IEEE Transactions on Microwave Theory and Techniques* **39**, 910 (1991).

⁸M. Gppl, A. Fragner, M. Baur, R. Bianchetti, S. Filipp, J. M. Fink, P. J. Leek, G. Puebla, L. Steffen, and A. Wallraff, *Journal of Applied Physics* **104**, 113904 (2008), <https://doi.org/10.1063/1.3010859>.

⁹E. U. Manual, Inc., Liverpool, NY (2008).

¹⁰D. J. Thoen, B. G. C. Bos, E. A. F. Haalebos, T. M. Klapwijk, J. J. A. Baselmans, and A. Endo, *IEEE Transactions on Applied Superconductivity* **27**, 1 (2017).

¹¹A. Endo, K. Karatsu, A. P. Laguna, B. Mirzaei, R. Huiting, D. Thoen, V. Murugesan, S. J. C. Yates, J. Bueno, N. V. Marrewijk, S. Bosma, O. Yurduseven, N. Llombart, J. Suzuki, M. Naruse, P. J. de Visser, P. P. van der Werf, T. M. Klapwijk, and J. J. A. Baselmans, *Journal of Astronomical Telescopes, Instruments, and Systems* **5**, 1 (2019).

¹²D. C. Mattis and J. Bardeen, *Phys. Rev.* **111**, 412 (1958).

¹³E. F. C. Driessen, P. C. J. J. Coumou, R. R. Tromp, P. J. de Visser, and T. M. Klapwijk, *Phys. Rev. Lett.* **109**, 107003 (2012).

¹⁴R. M. J. Janssen, J. J. A. Baselmans, A. Endo, L. Ferrari, S. J. C. Yates, A. M. Baryshev, and T. M. Klapwijk, *Applied Physics Letters* **103**, 203503 (2013), <https://doi.org/10.1063/1.4829657>.

¹⁵J. van Rantwijk, M. Grim, D. van Loon, S. Yates, A. Baryshev, and J. Baselmans, *IEEE Transactions on Microwave Theory and Techniques* **64**, 1876 (2016).

¹⁶S. J. C. Yates, A. M. Baryshev, O. Yurduseven, J. Bueno, K. K. Davis, L. Ferrari, W. Jellema, N. Llombart, V. Murugesan, D. J. Thoen, and J. J. A. Baselmans, *IEEE Transactions on Terahertz Science and Technology* **7**, 789 (2017).

¹⁷S. Hähnle, J. Bueno, R. Huiting, S. J. C. Yates, and J. J. A. Baselmans, *Journal of Low Temperature Physics* (2018), 10.1007/s10909-018-1940-1.

¹⁸TERABEAM 1550 (TOPTICA Photonics AG, Lochhamer Schlag 19, 82166 Gräfelfing, Germany).

¹⁹R. Barends, N. Vercruyssen, A. Endo, P. De Visser, T. Zijlstra, T. Klapwijk, P. Diener, S. Yates, and J. Baselmans, *Applied Physics Letters* **97**, 023508 (2010).

	Parameter	Value
Superconductor	T_c	14.7 K
	ρ_N	102 $\mu\Omega\text{cm}$
CPW geometry	s	1.95 μm
	w	2.15 μm
	t	100 nm
Experimental Setup	T	0.25 K
	f	320..380 GHz

TABLE I. Parameter definitions: T_c is the critical temperature of the superconductor. ρ_N is the superconductors normal state resistivity. The CPW is determined by the line width s , the slot width w and the film thickness t . Additional dependencies are on the system temperature T and measurement frequency f .

Appendix A: Characterization of a superconducting Coplanar Waveguide

The impedance Z_0 and effective dielectric constant ϵ_{eff} of a superconducting Coplanar Waveguide (CPW) can be calculated analytically by evaluating the CPW geometry and the superconductor properties independently, using only the parameters in Table I.

These parameters can be easily obtained from experiment with SEM (Scanning Electron Microscope) images of the CPW and DC property measurements of the superconductor. Characterizing the CPW is then split into two parts: First, calculate the surface impedance of the superconductor. Second, calculate the CPW properties using the surface impedance as input.

1. Superconductor

According to Mattis-Bardeen theory¹, based on the microscopic BCS theory of superconductivity², one can define a conductivity for the superconductor

$$\sigma = \sigma_1 - i\sigma_2 \quad (\text{A1})$$

analogous with Ohm's law $J = \sigma E$. The real and imaginary parts of the conductivity are given by integrals as

$$\begin{aligned} \frac{\sigma_1}{\sigma_N} &= \frac{2}{\hbar\omega} \int_{\Delta}^{\infty} |f(E) - f(E + \hbar\omega)| g_1(E) dE \\ &+ \frac{1}{\hbar\omega} \int_{\min(\Delta - \hbar\omega, -\Delta)}^{-\Delta} |1 - 2f(E + \hbar\omega)| g_1(E) dE \end{aligned} \quad (\text{A2})$$

$$\frac{\sigma_2}{\sigma_N} = \frac{1}{\hbar\omega} \int_{\max(\Delta - \hbar\omega, -\Delta)}^{\Delta} |1 - 2f(E + \hbar\omega)| g_2(E) dE \quad (\text{A3})$$

where $\omega = 2\pi f$, $\sigma_N = 1/\rho_N$ is the normal state conductivity, $\Delta \approx 1.76k_B T_c$ is the superconductors gap energy, $f(E)$ is the density of states generally given by the Fermi-Dirac distribution,

$$f(E) = \frac{1}{1 + \exp(E/k_B T)} \quad (\text{A4})$$

and $g_1(E)$ and $g_2(E)$ are defined as

$$g_1(E) = \frac{E^2 + \Delta^2 + \hbar\omega E}{(E^2 - \Delta^2)^{1/2} [(E + \hbar\omega)^2 - \Delta^2]^{1/2}} \quad (\text{A5})$$

$$g_2(E) = \frac{E^2 + \Delta^2 + \hbar\omega E}{(\Delta^2 - E^2)^{1/2} [(E + \hbar\omega)^2 - \Delta^2]^{1/2}}. \quad (\text{A6})$$

The second integral in σ_1 describes the pair-breaking process of Cooper pairs when $\hbar\omega \geq 2\Delta$ and is zero for frequencies below the gap frequency.

From the complex conductivity, the surface impedance then follows from³ as

$$Z_s = \sqrt{\frac{i\mu_0\omega}{\sigma}} \coth(t\sqrt{i\omega\mu_0\sigma}) = R_s + i\omega L_s \quad (\text{A7})$$

given in $[Z_s] = \Omega/\square$ with the surface resistance R_s and the surface inductance

$$L_s = \frac{\text{Im}(Z_s)}{\omega}. \quad (\text{A8})$$

This surface inductance is due to the acceleration of cooper pairs in an AC field while the surface resistance is dependent on the number of unpaired electrons (quasiparticles) in the superconductor. The resulting L_s , which is shown exemplary in Fig. 1 for the values given in Table I, has a frequency dependence which is negligible for $\hbar\omega \ll \Delta$, but becomes significant for $\hbar\omega \gtrsim \Delta/3$. While various simplifications for the calculation of L_s are possible, these usually break down in the limit of thin films and/or high frequencies and generally do not reproduce this frequency dependence.

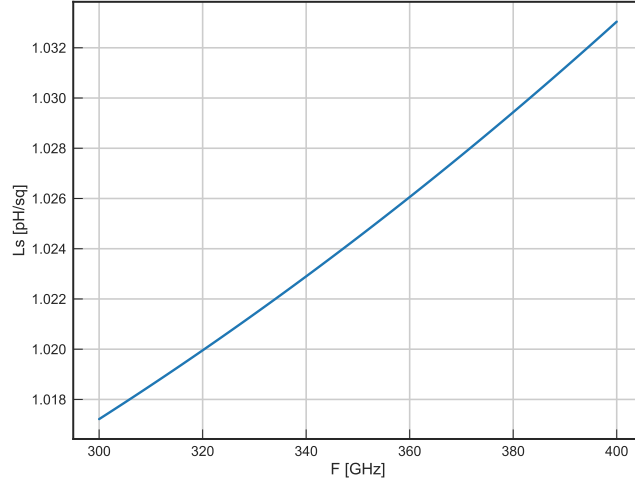


FIG. 1. Frequency dependent surface inductance calculated using the values in table I

2. Superconducting CPW

In a superconducting CPW, an effective dielectric constant can be determined from its phase velocity v_{ph} as

$$\epsilon_{eff} = \frac{c^2}{v_{ph}^2} = c^2(L_g + L_k)C_l. \quad (\text{A9})$$

with the line capacitance C_l , the geometric inductance L_g and the kinetic inductance L_k , all given per unit length. Equivalently, the characteristic impedance is given by

$$Z_0 = \sqrt{\frac{L_g + L_k}{C_l}} \quad (\text{A10})$$

The line capacitance and geometric inductance are determined by the dimensions of the CPW and are given by

$$L_g = \frac{\mu_0 K(k')}{4K(k)} \quad (\text{A11})$$

$$C_l = 4\epsilon_0\epsilon_{eff,geo} \frac{K(k)}{K(k')} \quad (\text{A12})$$

where $k = s/(s + 2w)$, $k'^2 = 1 - k^2$, K is the complete elliptic integral of the first kind and $\epsilon_{eff,geo} \approx (1 + \epsilon_{subs})/2$ is the effective dielectric constant visible to the line capacitance due to the substrate below the CPW line.

The kinetic inductance L_k is dependent on both the superconductor properties and the CPW geometry and can be calculated analytically as

$$L_k = g_c L_{s,c} + g_g L_{s,g} \quad (A13)$$

where $L_{s,c}$ and $L_{s,g}$ are the surface inductances of the central line and groundplane as given by eqs.A7 and A8, and g_c and g_g their respective geometry factors⁴

$$g_c = \frac{1}{4s(1 - k^2)K^2(k)} \left[\pi + \ln \left(\frac{4\pi s}{t} \right) - k \ln \left(\frac{1 + k}{1 - k} \right) \right] \quad (A14)$$

$$g_g = \frac{1}{4s(1 - k^2)K^2(k)} \left[\pi + \ln \left(\frac{4\pi(s + 2w)}{t} \right) - \frac{1}{k} \ln \left(\frac{1 + k}{1 - k} \right) \right]. \quad (A15)$$

The geometry factors were originally described in *Foundations for Microwave Engineering* by R.E.Collin⁵ for the losses in the central line and groundplane of a CPW, and have been intuitively adapted to apply for the kinetic inductance contribution. This adaptation has been verified by comparison with simulations, e.g. Sonnet, and has been found to be in excellent agreement with experimental results over the last years. In the case of a single film CPW with surface inductance $L_s = L_{s,c} = L_{s,g}$, eq. A9 can then be rewritten as

$$\epsilon_{eff} = c^2(L_g + gL_s)C_l \quad (A16)$$

with $g = g_c + g_g$.

Figure 2 shows the effective dielectric constant as a function of frequency for the values given in Table I, where a large kinetic inductance is achieved by choosing a superconductor with large L_s , corresponding to a high resistivity and thin film, and designing a narrow CPW with large g . In this configuration, the ϵ_{eff} is dominated by the kinetic inductance, showing the same frequency dependence.

Finally, the internal quality factor of a superconducting CPW due to ohmic losses from quasiparticles is given by

$$Q_i = \frac{1}{\alpha_k} \frac{\omega L_s}{R_s} \quad (A17)$$

with the kinetic inductance fraction $\alpha_k = L_k/(L_g + L_k)$. For the given example values, we obtain $Q_i \approx 10^{49}$, which is negligible compared to other loss sources.

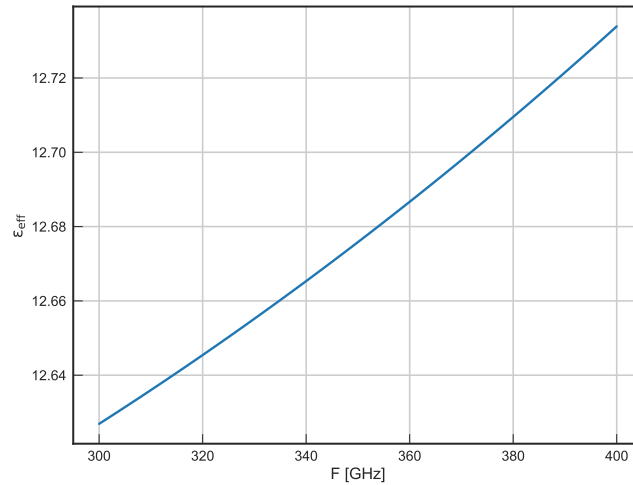


FIG. 2. Frequency dependent dielectric constant calculated using the values in table I

Appendix B: Simulating an on-chip Fabry-Pérot Resonator

The Fabry-Pérot resonator (FP) is very long compared to the relevant wavelengths ($L_{FP} \gtrsim 40\lambda$) with feature sizes much smaller than a wavelength, due to the narrow line. This makes a simulation of the full structure impractical due to the required fine mesh and large box size. It is therefore preferable to split the resonator into its separate components, i.e. the coupling structures and the transmission line, and cascade them using ABCD matrices. Three simulation setups to determine the coupling strength as well as the radiation loss of both transmission line and coupler will be shown here. All simulations are performed in Sonnet⁶, which is a commercial 3D planar EM software capable of simulating superconducting structures at high frequencies.

1. Coupler Simulation

The coupler is simulated in a small box of $32 \times 32 \mu\text{m}^2$ as shown in Fig. 3a), resulting in the scattering matrix S , with S_{21} shown in Fig. 3b) as function of frequency. The box size is chosen as small as possible without impacting the simulation result. Both top and bottom of the box are defined as lossless metal, with a layer of vacuum above and a layer of lossless Sapphire below the metalization with $h_{diel} = 500 \mu\text{m}$ for both layers. Superconducting NbTiN is implemented using the "general model" with zero resistance and a finite surface impedance L_s . A lookup table with the frequency dependence for L_s , generated using Appendix A, is used as input for the model.

The coupling structure is implemented as an overlapping coupler with a short to ground, where the coupling strength can be tuned by changing the overlap parameter p . Port 1 on the left side is connecting to either the antenna or the detector, while port 2 is part of the FP resonator. The position of the overlapping slots is adjusted for different CPW line widths on the resonator side to keep $s_0 = 2 \mu\text{m}$ constant. Due to the frequency dependence of L_s and consequently the line impedance Z_0 , the line will be slightly mismatched with the constant port impedance Z_p . To account for this, a reference plane close to the coupler is used and the port impedances are set to 50Ω . The scattering matrix for the correct port impedance is then retrieved in post processing. This also makes optimization in the design phase easier, as the port impedance does not need to be adjusted in the simulation setup if the line impedance changes.

In order to obtain the coupler geometry for a desired Q_c of the FP resonator, a sweep of p is performed from 300 to 400 GHz, using a cell size of $0.5 \mu\text{m}$ with the smallest feature size of $2 \mu\text{m}$. The simulations for the fabricated chips are carried out with the measured dimensions and a cell size of $0.05 \mu\text{m}$ to sample the overetched geometry.

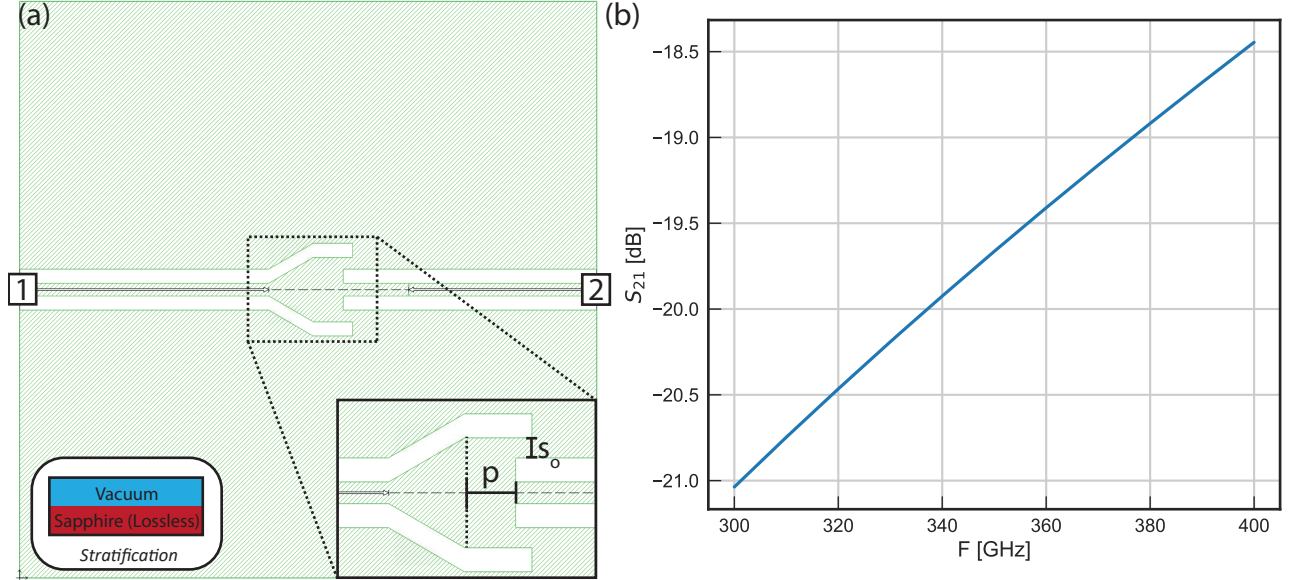


FIG. 3. (a) Sonnet box of the coupler simulation with inset showing the stratification and a zoom-in on the the coupling structure. NbTiN is shown in green; substrate in white. (b) Simulated S_{21} of the measured chip, where $s = 1.95 \mu\text{m}$ and $w = 2.15 \mu\text{m}$. Output from Sonnet, with 50Ω port impedance.

Box size [μm^2]	2048×2048
Cell size [μm^2]	0.5×0.5
Groundplane width [μm]	400
CPW length [μm]	800..1800
Vacuum layer thickness	$\lambda_0/4$
Lossless substrate thickness [μm]	100
Lossy substrate thickness [μm]	100,000
Loss tangent	1
F [GHz]	350

TABLE II. Parameters used for the radiation loss simulation.

2. Radiation Loss Simulation

a. CPW line loss

Retrieving radiation loss of any structure in Sonnet requires a careful setup of the simulation. Any loss in the structure corresponds to power that does not reach the ports of the simulation and can therefore be obtained from the scattering matrix as

$$P_{rad} = 1 - P_{out} = 1 - (|S_{11}|^2 + |S_{21}|^2). \quad (\text{B1})$$

The Sonnet box used to simulate the radiation loss in a CPW, shown in Fig. 4, fulfills the following requirements for an accurate result:

- The structure is able to radiate freely.
- Radiated power is not absorbed in the ports.
- The structure is otherwise lossless (e.g. ohmic losses, dielectric losses).

The CPW can radiate when the propagating field can couple to modes in the surrounding media, i.e. the vacuum above and the Sapphire substrate below. However, the lossless metal walls of the Sonnet box act as a waveguide with a cut-off frequency given by the box size, below which no modes can be excited. Therefore, the box is made sufficiently large compared to the freespace wavelength λ_0 ($Y_{box} = X_{box} \gtrsim 2\lambda_0 = 2048 \mu\text{m}$) to allow all relevant modes to be excited. All relevant dimensions used in the simulation are also summarized in table B 2 a

The simulation is set up as shown in Fig. 4a) with superconducting NbTiN and a $100 \mu\text{m}$ thick lossless Sapphire substrate equivalent to section B 1, resulting in no ohmic or dielectric losses. However, for a fully enclosed lossless metal box with no lossy components, any radiated power will be reflected back and eventually absorbed in one of the ports and result in $P_{rad} = 0$. To avoid this in the Sonnet simulation, the top and bottom walls are set to free space, where radiation at the boundary is absorbed. However, surface waves in the Sapphire substrate are still confined by reflections at the sidewall. A thick lossy layer of Sapphire is placed below the lossless layer in order to attenuate these surface waves, before they can be absorbed in the ports. Ports are set up as co-calibrated internal ports in a push-pull configuration with a floating ground connection (see Fig. 4a)) and without de-embedding. To avoid reflections, the port impedance is set to the line impedance, which is retrieved from a separate simulation. The metalization is confined to a patch in the middle of the box such that the sidewalls do not affect the radiating structure. Finally, the vacuum layer above the CPW needs to be precisely $\lambda_0/2$ thick, otherwise numerical issues arise in the simulation.

In summary, the following design rules need to followed:

- A large box size compared to the wavelength $Y_{box} = X_{box} \gtrsim 2\lambda_0$.
- The top and bottom wall of the box are free space.
- A precise vacuum layer thickness above the metalization $t_{vac} = \lambda_0/2$.
- Two layers of substrate, one lossless layer ($\tan \delta = 0$) of medium thickness directly below the metalization and one lossy, very thick layer ($\tan \delta = 1$) below that.
- Co-calibrated internal ports with a floating ground connection.

- The superconductor is a metal using the general model with L_s set as the surface inductance in pH/\square .

To make certain that the simulated P_{rad} is not affected by any other systematic errors in the simulation, a sweep of the CPW length L_{cpw} is performed and a linear fit through the resulting $P_{rad}(L_{cpw})$ is used to determine the loss factor α , as shown in Fig. 4b). The groundplane can be kept at a constant width for this purpose. The corresponding internal quality factor is then given by $Q_i = \beta/(2\alpha)$, with $Q_i = 15100$ for the narrowest line with $s = w = 2 \mu\text{m}$.

This simulation method was verified by comparing a PEC simulation ($L_s = 0 \text{ pH}/\square$) with analytical models, which found good agreement as shown in Fig. 4c). Additionally, good agreement was found with simulations of superconducting CPW carried out in the 3D EM software CST⁷.

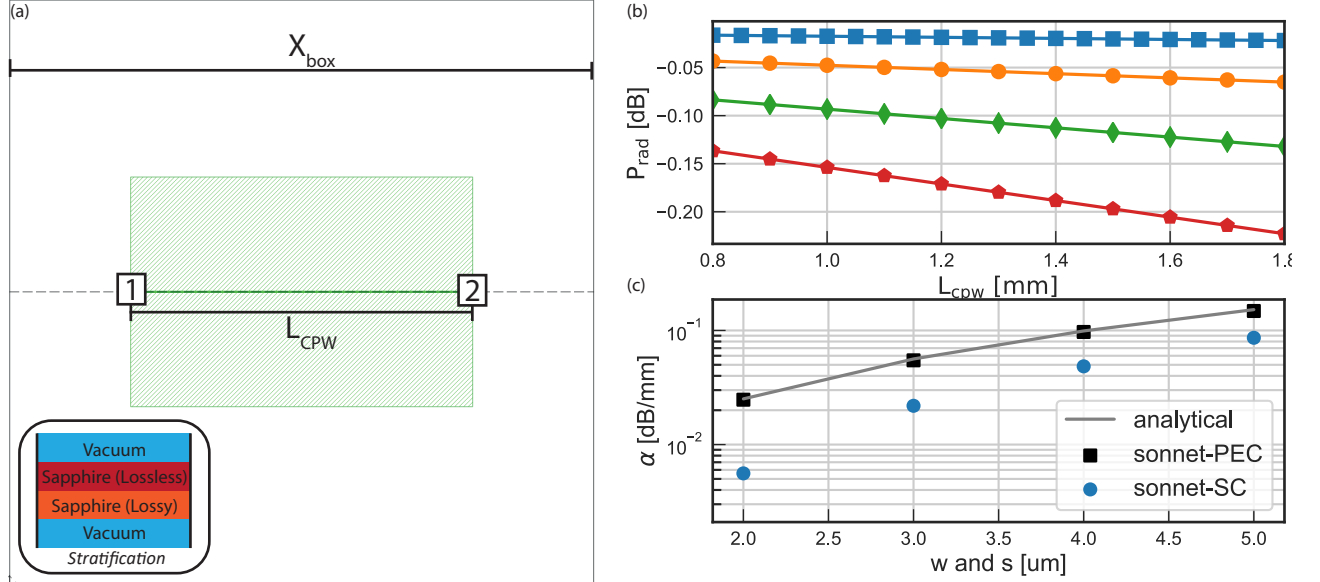


FIG. 4. (a) Sonnet box to simulate the radiation loss of a straight CPW line with inset showing the stratification of the dielectric layers. (b) Simulated loss as function of line length for different NbTiN CPWs where $s=w$ ($2 \mu\text{m}$: blue; $3 \mu\text{m}$: orange; $4 \mu\text{m}$: green; $5 \mu\text{m}$: red). The Straight lines are linear fits. (c) Loss factor alpha as function of CPW line width. Sonnet-SC corresponds to the fitted values of plot (b). Sonnet-PEC is compared to the analytical solution for a PEC CPW, showing good agreement.

b. Resonator loss

While a full length FP resonator is too large to implement in Sonnet, shorter resonators can be simulated as shown in Fig 6a) to obtain the loss at a given frequency as function of mode number. For this purpose, the same box as in section B 2 a is used, but the simple straight line is exchanged for a 2-port FP resonator with the couplers as designed in B 1 and a resonator length such that

$$L_{res} = n \frac{c}{2F\sqrt{\epsilon_{eff}}} \quad (\text{B2})$$

with the resonance frequency $F = 350 \text{ GHz}$, the dielectric constant of the line ϵ_{eff} and the mode number n , which is varied from 1 to 14. The simulation for each mode number is carried out in a small range around the resonance frequency, resulting in a S_{21} peak which is dependent on mode number as shown in Fig. 5b) for a CPW with $s = w = 2 \mu\text{m}$. The downshift in resonance frequency at small mode numbers, shown in Fig. 5b), is due to the coupling inductance, which represents a larger fraction of the total resonator inductance for shorter resonators. The loaded quality factor Q_L of the peak is given by

$$\frac{1}{Q_L} = \frac{1}{Q_i} + \frac{1}{Q_c} = \frac{1}{Q_{i,l}} + \frac{1}{Q_{i,c}} + \frac{1}{Q_c} \quad (\text{B3})$$

with the coupling strength Q_c , the internal loss of the line $Q_{i,l}$ and the loss at the coupler $Q_{i,c}$. Both $Q_{i,c}$ and Q_c are linear in mode number and can be expressed as $Q_{i,c} = nQ_{i,c1}$ and $Q_c = nQ_{c1}$, where the index 1 corresponds to

the value at $n = 1$. This can be intuitively understood as a reduced impact of the coupler on the resonator behaviour when the resonator becomes longer than the wavelength. The peak height of the resonator is given by

$$|S_{21}^{max}| = \frac{Q_L}{Q_c}, \quad (\text{B4})$$

and can therefore be used to distinguish between internal losses and the coupling strength. Fitting Q_c and Q_i results in $Q_{c1} = 212$, $Q_{i,c1} = 1307$ and $Q_{i,l} = 16980$. As $Q_{i,l}$ is independent of mode number, the resonator is in a Q_c limited regime for low n and transitions to a $Q_{i,l}$ dominated regime at high n , while $Q_{i,c}$ is negligible in both regimes. The obtained value for $Q_{i,l}$ shows good agreement with the pure line simulation of $Q_i = 15100$ in section B 2 a. Slight deviations between these two values are expected, as a resonating structure has a different current distributions compared to a simple straight line, thus affecting the radiating fields.

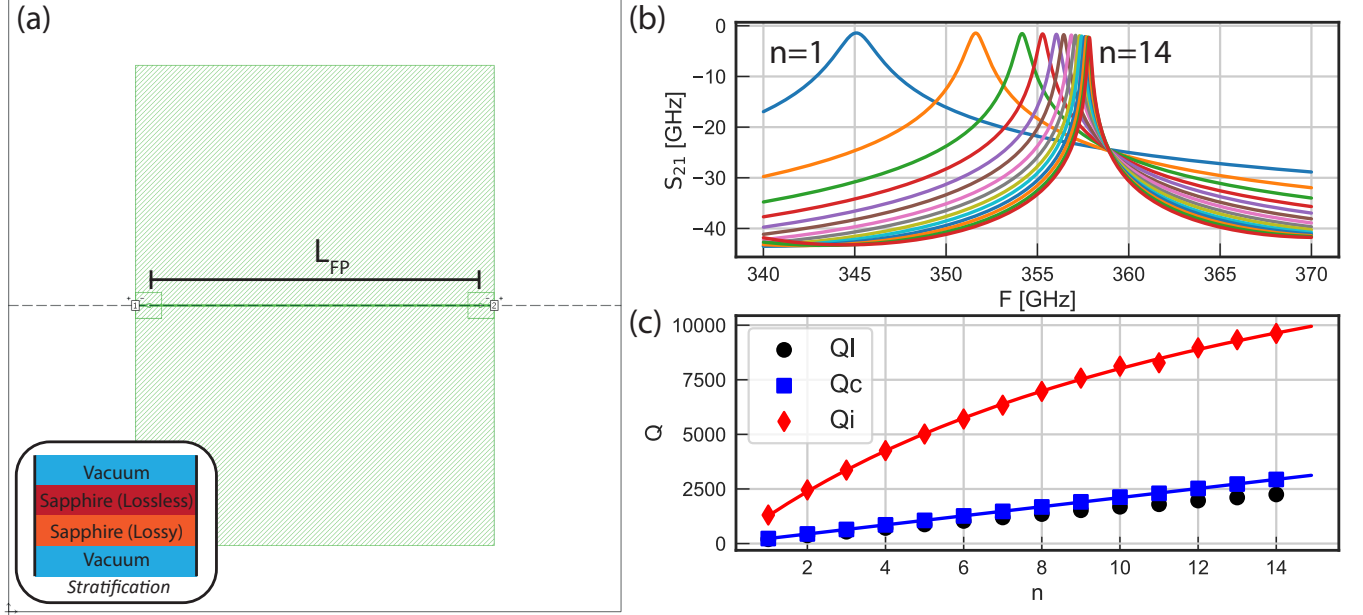


FIG. 5. (a) Sonnet box to simulate the radiation loss of a short Fabry-Pérot resonator, with inset showing the stratification of the dielectric layers. (b) Simulated S_{21} for different resonator lengths, corresponding to different mode numbers n . (c) Quality factors extracted from the peaks in figure b shown as points with fits for Q_i and Q_c shown as lines.

3. ABCD-Matrix method

The transmission S_{21} through the Fabry-Pérot resonator can be obtained by splitting it into separate network elements, solving their individual behaviour, and then cascading the resulting ABCD matrices⁸

$$M_{FP} = M_{C1} M_{CPW} M_{C2} = \begin{bmatrix} A & B \\ C & D \end{bmatrix} \quad (\text{B5})$$

where M_{FP} is the ABCD matrix of the full resonator and M_{C1} , M_{CPW} , M_{C2} correspond to the couplers and CPW line as shown in Fig. 6. This approach requires the use of ABCD matrices, as scattering matrices can not be cascaded in this way.

The individual ABCD matrices are given as:

$$M_{C1} = M_{C2} = \begin{bmatrix} \frac{(1+S_{1'1'}) (1-S_{2'2'}) + S_{1'2'} S_{2'1'}}{2S_{2'1'}} & Z_p \frac{(1+S_{1'1'}) (1+S_{2'2'}) - S_{1'2'} S_{2'1'}}{2S_{2'1'}} \\ \frac{1}{Z_p} \frac{(1-S_{1'1'}) (1-S_{2'2'}) - S_{1'2'} S_{2'1'}}{2S_{2'1'}} & \frac{(1-S_{1'1'}) (1+S_{2'2'}) + S_{1'2'} S_{2'1'}}{2S_{2'1'}} \end{bmatrix} \quad (\text{B6})$$

where S_{ij} and Z_p are the scattering parameters and the port impedance of the coupler simulation as given in section

B 1, and

$$M_{CPW} = \begin{bmatrix} \cosh(\gamma L_{FP}) & Z_{0,cpw} \sinh(\gamma L_{FP}) \\ \frac{1}{Z_{0,cpw}} \sinh(\gamma L_{FP}) & \cosh(\gamma L_{FP}) \end{bmatrix}. \quad (B7)$$

where $Z_{0,cpw}$ is the characteristic impedance of the FP line, L_{FP} is the resonator length and $\gamma = \alpha + i\beta$ is the complex propagation constant with the loss factor α and the propagation constant β . The loss factor α can be obtained from the simulation of section B 2 a, while $Z_{0,cpw}$ and β can be obtained either from simulation or analytically as described in section A.

The transmission S_{21} through the resonator can then be retrieved from eq. B5

$$S_{21} = \frac{2(AD - BC)}{A + B/Z_0 + CZ_0 + D} \quad (B8)$$

where Z_0 is the characteristic impedance of the transmission line outside the resonator, assuming the lines to the antenna and the detector are identical. The resulting spectrum using the example simulations from sections B 1 and B 2 a with a resonator length of $L_{FP} = 10$ mm is shown in Fig.7, clearly showing the characteristic peaks of the Fabry-Pérot, with a reduced peak height due to the lossy CPW.

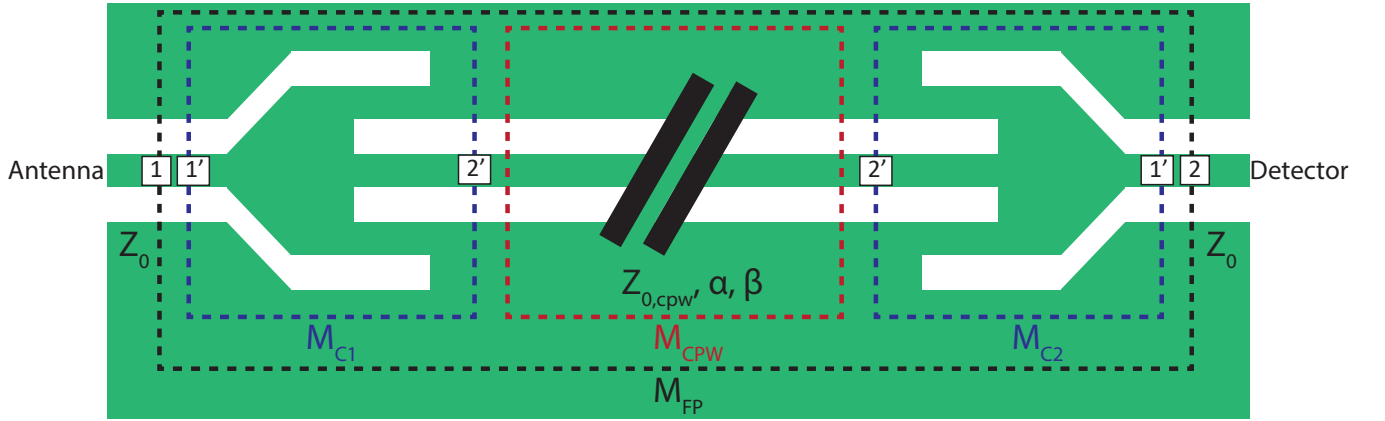


FIG. 6. Schematic of a Fabry-Pérot resonator split into its individual components with associated ABCD matrices.

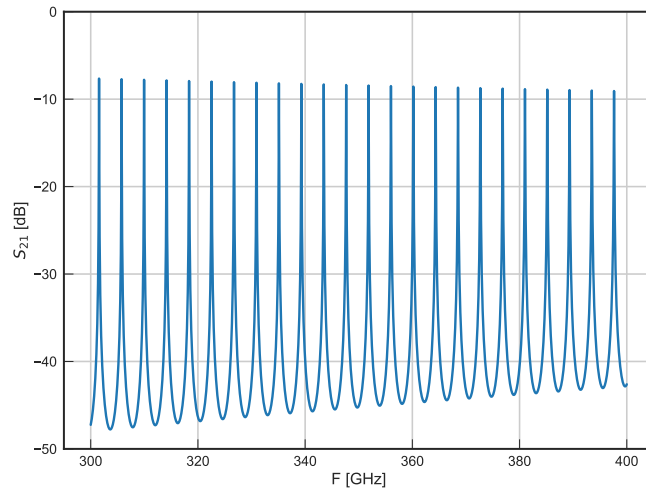


FIG. 7. Calculated Fabry-Pérot transmission based on Sonnet simulations of the coupling strength and radiation loss for a CPW with $s = 1.95 \mu\text{m}$ and $w = 2.15 \mu\text{m}$.

- ¹D. C. Mattis and J. Bardeen, Phys. Rev. **111**, 412 (1958).
- ²J. Bardeen, L. N. Cooper, and J. R. Schrieffer, Phys. Rev. **108**, 1175 (1957).
- ³R. L. Kautz, Journal of Applied Physics **49**, 308 (1978).
- ⁴P. J. de Visser, *Quasiparticle dynamics in aluminium superconducting microwave resonators*, Ph.D. thesis.
- ⁵R. E. Collin, *Foundations for Microwave Engineering*, McGraw-Hill series in electrical engineering (McGraw-Hill, 1992).
- ⁶E. U. Manual, Inc., Liverpool, NY (2008).
- ⁷A. Pascual Laguna, private communication.
- ⁸D. M. Pozar, *Microwave engineering; 4th ed.* (Wiley, Hoboken, NJ, 2011).